A&A, 707, A219 (2026)
https://doi.org/10.1051/0004-6361/202557601

Astronomy & Astrophysics

Is the high-energy environment of K2-18b special?

S. Rukdee[1,⋆], M. Güdel[2], I. Vilović[3], K. Poppenhäger[3,4], S. Boro Saikia[2], J. Buchner[1], B. Stelzer[5], G. Roccetti[6,7], J. V. Seidel[8,9], and V. Burwitz[1]

[1] Max Planck Institute for Extraterrestrial Physics, Giessenbachstrasse 1, 85748 Garching, Germany
[2] Department of Astrophysics, University of Vienna, Türkenschanzstr. 17, 1180 Vienna, Austria
[3] Leibniz-Institute for Astrophysics Potsdam (AIP), An der Sternwarte 16, 14482 Potsdam, Germany
[4] Potsdam University, Institute for Physics and Astronomy, Karl-Liebknecht-Str. 24/25, 14476 Potsdam-Golm, Germany
[5] Institut für Astronomie und Astrophysik, Eberhard Karls Universität Tübingen, Sand 1, 72076 Tübingen, Germany
[6] European Southern Observatory, Karl-Schwarzschild-Straße 2, 85748 Garching near Munich, Germany
[7] Meteorologisches Institut, Ludwig-Maximilians-Universität München, Munich, Germany
[8] European Southern Observatory, Alonso de Córdova, 3107 Vitacura, Región Metropolitana, Chile
[9] Laboratoire Lagrange, Observatoire de la Côte d'Azur, CNRS, Université Côte d'Azur, Nice, France

Received 8 October 2025 / Accepted 12 January 2026

ABSTRACT

Context. The exoplanet K2-18 b lies near the radius valley that separates super-Earths and sub-Neptunes, marking a key transitional regime in planetary and atmospheric composition. The system offers a valuable opportunity to study how M-dwarf high-energy stellar radiation influences atmospheric stability and the potential for sustaining volatile species, which is especially important in the context of the upcoming ELT and its ANDES spectrograph.
Aims. This study characterizes the high-energy environment of K2-18 with X-ray observations from eROSITA, the soft X-ray instrument on the Spectrum-Roentgen-Gamma mission, *Chandra*, and *XMM-Newton*.
Methods. We derived a representative 0.2–2 keV X-ray flux with an APEC thermal plasma model fit with the Bayesian X-ray Analysis (BXA). With the observed X-ray flux from the exoplanet host star, we estimated the photoevaporative mass loss of exoplanet K2-18b using the energy-limited model. In addition, we examined the thermal structure of the system based on a hydrodynamic model.
Results. In a 100 ks *XMM-Newton* observation, we identified K2-18 as a very faint X-ray source with $F_X = 10^{-15}$ erg s^{-1} cm^{-2} and an activity level of (Lx/Lbol) ~10^{-5}. A small flare was detected during the observation. The planet is irradiated by an X-ray flux of $F_{pl,X} = 12 \pm 3$ erg s^{-1} cm^{-2}.
Conclusions. The X-ray flux measurement of K2-18 gives important limitations for the atmospheric escape and photochemical modeling of its exoplanets. Despite its near orbit around an M-dwarf star, K2-18b's low-activity-level environment suggests that it can retain an atmosphere, supporting recent tentative detections of atmospheres.

Key words. planets and satellites: atmospheres – planet-star interactions – stars: low-mass – stars: individual: K2-18 – X-rays: stars

1. Introduction

High-energy radiation from an exoplanet's host star can cause a planet's atmospheric evaporation (Lammer et al. 2003; Vidal-Madjar et al. 2003; Ehrenreich & Désert 2011; Johnstone et al. 2018; Yan & Henning 2018; Poppenhaeger et al. 2021; Foster et al. 2022; Fromont et al. 2024). Understanding the host star's X-ray and ultraviolet (XUV) flux, combined with modeling, helps determine its impact on atmospheric escape, chemistry, and long-term atmospheric evolution (Becker et al. 2020; Johnstone et al. 2021b; Amaral et al. 2025; McCreery et al. 2025; Van Looveren et al. 2025). Many small planets discovered to date are around low-mass M-type stars (Howard et al. 2012; Dressing & Charbonneau 2013). The long pre-main-sequence lifetime of M stars implies that they remain strongly magnetically active much longer than a G star (Ramirez & Kaltenegger 2014). Close proximity of exoplanets to their host stars therefore increases the risk of high-energy radiation affecting their physical and chemical properties. Multiple studies identify XUV radiation from M dwarfs as a potential threat to planetary habitability (Heath et al. 1999; Tarter et al. 2007; Lammer et al. 2009; Shields et al. 2016; Meadows et al. 2018; Van Looveren et al. 2024, 2025). M dwarfs are known for their frequent and intense flares (e.g., Loyd et al. 2018; Günther et al. 2020). Strong flares from an M-dwarf host star can significantly alter the chemistry of a planet's atmosphere and may lead to its removal (Güdel et al. 2002; Segura et al. 2010). Early *James Webb* Space Telescope (JWST) results suggest that temperate rocky exoplanets around M dwarfs do not retain substantial atmospheres (Greene et al. 2023; Zieba et al. 2023; Cadieux et al. 2024). These observations have meanwhile been explained using atmospheric mass-loss models (Van Looveren et al. 2025). For instance, the Sun produces its most energetic flares (~10^{32} erg) about once per solar cycle (Lin 1994; Aulanier et al. 2013; Youngblood et al. 2017), whereas M dwarfs can emit flares of similar energy daily (Audard et al. 2000). Even flares from magnetically inactive early M-type stars, which exhibit fewer starspots and less frequent flaring, can significantly influence the atmospheric chemistry of orbiting planets (Hawley et al. 2014). Previous studies show that M dwarfs exhibit lower X-ray luminosities compared to G stars at any age, but they take longer to desaturate in terms of Lx/Lbol, especially late M dwarfs (Magaudda et al. 2020; Johnstone et al. 2021a).

⋆ Corresponding author: `suri@mpe.mpg.de`

A recent study (Zhu & Preibisch 2025) of neighboring GKM stars finds that the majority (≥60%) of nearby M dwarfs no later than M6 have X-ray activity ($\log(L_X/L_{\rm bol})$) levels that are not higher than the average (80th percentile) recorded in G-type stars. The considerable diversity of stars and their exoplanets motivates detailed characterization of individual systems.

Differences between UV and X-ray emissions in the high-energy environment indicate various physical processes occurring in different layers of the stellar atmosphere. UV radiation is largely emitted by the chromosphere and transition region of stars, where temperatures range from thousands to tens of thousands of Kelvin. Magnetic activity and ionization processes heat these locations (France et al. 2016; Ribas 2009). The corona, the outermost and hottest layer of the stellar environment, generates X-rays at temperatures of millions of Kelvin. X-rays are produced by very energetic processes such as magnetic reconnection, which leads to plasma heating (Shoda & Takasao 2021; Maggio et al. 2023). Accurate observations across the UV and X-ray bands are critical for understanding the physical mechanisms that drive star emissions.

The wavelength-dependent photoabsorption cross-sections of atoms and molecules cause diverse heating and chemical processes across the planetary atmospheric layers. In high-energy environments, near-UV (1800–3200 Å), far-UV (912–1800 Å), and X-ray (5–100 Å) photons are absorbed in the middle-to-upper atmosphere, photo-dissociating molecules, and ionizing heavy elements. EUV photons (100–911 Å) are absorbed higher in the thermosphere, ionizing atoms and molecules, which leads to both thermal and nonthermal atmospheric escape (France et al. 2016; Youngblood et al. 2016; Gronoff et al. 2020). Lyman-α (Lyα), commonly used as a proxy for high-energy UV flux, accounts for approximately 37%–75% of the total 1150–3100 Å flux in most M dwarfs (France et al. 2013).

The star K2-18 hosts an exoplanetary system (Montet et al. 2015) and is an excellent target for atmospheric studies. K2-18 is an M2.8 star with a rotation period of ∼38.6 days (Cloutier et al. 2017). Of particular interest is the planet K2-18b, which orbits the star with a period of 33 days at a semi-major axis of approximately 0.142 AU (Montet et al. 2015). A wide range of interior structure models have been proposed for K2-18b, involving different proportions of H_2O and H_2/He in a volatile-rich atmosphere. These scenarios were followed up by observations (Madhusudhan et al. 2023) revealing ∼1% CO_2, ∼1% CH_4, and non-detections of CO and NH_3, as shown in Fig. 1 in Luu et al. (2024). Similar abundances of CO_2 and CH_4 were also reported by Hu, et al. (2025). Proposed scenarios include a thin-atmosphere rocky world (Tsai et al. 2021; Yu et al. 2021), a thin-atmosphere water world sometimes referred to as a “Hycean” world (Piette & Madhusudhan 2020; Madhusudhan et al. 2021, 2023; Cooke & Madhusudhan 2024; Tsai et al. 2024; Wogan et al. 2024), a deep-atmosphere mini-Neptune lacking a solid surface (Hu et al. 2021; Tsai et al. 2021; Yu et al. 2021; Wogan et al. 2024), and a magma ocean mini-Neptune (Shorttle et al. 2024). A rocky-world scenario appears inconsistent with current observations (Madhusudhan et al. 2020), primarily due to the planet’s bulk density ($2.67^{+0.52}_{-0.47}$ g/cm^2 from Benneke et al. 2019) and atmospheric composition. In contrast, the thin-atmosphere water world and mini-Neptune scenarios remain plausible. Nonetheless, the Hycean scenario itself is questioned by the community, even under the assumptions of the abundances derived in Madhusudhan et al. (2023) (e.g., Wogan et al. 2024; Huang et al. 2024; Shorttle et al. 2024; Werlen et al. 2025).

Among these interior studies, the Stratified Mini-Neptune model (Benneke et al. 2024) proposes a homogeneous supercritical H_2–H_2O ocean at pressures from 1–5 kbar, which is consistent with the observed CH_4/CO_2 ratio. The phase-separated mini-Neptune scenario (Gupta et al. 2025) suggests that pressures of 5–10 kbar, H_2, and H_2O may be immiscible at some temperatures, resulting in a phase-separated water-rich layer underneath a supercritical H_2-rich layer. Additionally, Luu et al. (2024) proposed a global hydrothermal system where a supercritical water ocean interacts with the atmosphere. This model explains the observed CH_4/CO_2 ratio and the non-detection of CO, suggesting ocean temperatures ranging from 710 K to 1070 K. According to the decision tree roadmap for characterizing temperate sub-Neptunes of Hu, et al. (2025), K2-18b could fall into the category of a mixed steam envelope with nitrogen depletion.

For the atmospheric observation on K2-18b, Benneke et al. (2019) and dos Santos et al. (2020) previously suggested that K2-18b possesses an H_2-dominated envelope with potential HST detection of H_2O (Tsiaras et al. 2019). The EUV irradiation on K2-18b was estimated to lie in the range of 10^1-10^2 erg s^{-1} cm^{-2} from dos Santos et al. (2020). They find that under this EUV it is likely to lose only a small fraction of its mass (1% or less) over its remaining lifetime. The study suggested that the planet is probably not an archetypal planet crossing the radius valley (Fulton et al. 2017; Fulton & Petigura 2018; Van Eylen et al. 2018) to become a bare rock.

Recently, from the JWST near-infrared data, a tentative detection of the potential biomarkers dimethyl sulfide (DMS) and dimethyl disulfide (DMDS) was reported (Madhusudhan et al. 2025). On Earth, DMS is mainly produced by marine phytoplankton through biological processes (Madhusudhan et al. 2025). While these claimed detections of such complex molecules are unique in exoplanet studies –where focus is typically placed on simpler species such as H_2O, CO_2, and CH_4– it is important to note that the reported DMS claim in Madhusudhan et al. (2025) stems from a limited retrieval framework. As highlighted by Welbanks et al. (2025), the molecular input set in the original DMS detection was highly constrained, which significantly influenced the inferred composition and contributed to the ongoing debate over the potential biosignature claim. A reanalysis of the original detection data by Schmidt et al. (2025) found both the claimed detection of CO_2 and DMS unsubstantiated, while they were able to reproduce the CH_4 detection. Upon carrying out independent analyses to uncover statistically significant spectral features, Taylor (2025), Welbanks et al. (2025), and Stevenson et al. (2025) found no significant feature in the same JWST data. Most importantly, Luque et al. (2025) jointly analyzed NIRISS, NIRSpec, and MIRI data over the full panchromatic spectrum and found insufficient evidence for DMS or DMDS and that various molecules with methyl functional groups provide an equally good fit to the data. While the biomarker detection claim on K2-18 b has therefore been robustly discussed and subsequently dismissed by the community (Pica-Ciamarra et al. 2025; Luque et al. 2025; Welbanks et al. 2025; Taylor 2025), the debate on the detectability of potential biomarkers in exoplanets orbiting M dwarfs remains a main science driver in our field. In this context, understanding how K2-18 compares with other M dwarfs in terms of X-ray output is essential for assessing the long-term habitability of its planets, particularly K2-18b, and their suitability for more targeted observational campaigns. Indeed, a tentative distinction of DMS from a flat line fit would require ∼25 more MIRI transits (Luque et al. 2025), and only a holistic understanding of K2-

18b's space environment could potentially justify the extraordinary time commitment. Previous research has highlighted the potential for atmospheric characterization of K2-18b; however, direct constraints on its high-energy environment are limited due to the scarcity and low sensitivity of previous X-ray observations. Understanding the planet's atmospheric composition and chemistry is highly dependent on a precise understanding of the incident stellar flux, which has remained particularly unknown in the XUV regime.

High-resolution spectroscopic studies (Sairam & Madhusudhan 2025) of chromospheric lines (Hα, CaII H & K) show that K2-18 exhibits relatively low chromospheric activity, which is consistent with its rotation period and photometric variability, which indicated low activity during recent JWST observations. This quiet state is favorable for atmospheric characterization of K2-18b, as it minimizes contamination in transmission spectra and stellar variability. However, residual chromospheric activity may still contribute to the high-energy radiation environment. Long-term photometric monitoring further suggests the presence of an activity cycle (Sairam & Madhusudhan 2025), providing useful constraints for the planning of future spectroscopic follow-up of this system.

In this work, we revisited the high-energy environment of the star K2-18 to determine how long K2-18b can retain its atmosphere. Even if the atmosphere is not fully lost, its chemistry and haze formation are shaped by the stellar high-energy radiation, making it critical to study this environment to attain insights into both atmospheric escape and photochemical processes. By presenting new measurements of K2-18's X-ray flux, we aim to refine current models of atmospheric evolution and improve our understanding of habitability around low-mass stars. This is especially relevant in the context of future telescopes designed to evaluate the habitability of rocky exoplanets orbiting nearby M dwarfs, such as through reflected light observations with ANDES on the Extremely Large Telescope (ELT; Palle et al. 2025; Roccetti et al. 2025). In Sect. 2, we present new X-ray observations from different missions over the past four years. In Sect. 3, we describe the spectral extraction, spectral analysis, and modeling methods used to interpret the data. The results of the recent X-ray observations are shown in Sect. 4. We discuss these results in Sect. 5 and conclude in Sect. 6.

Star K2-18

The star K2-18 is located approximately 38.07 ± 0.08 pc from the Sun. It is classified as an M2.5V-type star (Schweitzer et al. 2019), with a mass of $0.413 \pm 0.043, \mathrm{M}_\odot$, a radius of $0.394 \pm 0.038, \mathrm{R}_\odot$, effective temperature of 3503 ± 60 K, and a metallicity of 0.09 ± 0.09 dex (Montet et al. 2015). Hejazi et al. (2024) used high-resolution spectroscopic data from IGRINS to derive abundance ratios of planet-building elements, including Al/Mg, Ca/Mg, Fe/Mg, and C/O. The C/O yields 0.568 ± 0.026. Later, Sairam & Madhusudhan (2025) used archival photometric and spectroscopic observations to estimate the star's effective temperature (T_eff) of 3645 ± 52 K and age of 2.9–3.1 Gyr. Their metallicity estimates ([Fe/H] = 0.10 ± 0.12 dex) are in good agreement with previous studies. Guinan & Engle (2019) adopted the age of 2.4 Gyr for K2-18 and used F_X-age and $F_{\mathrm{Ly}\alpha}$-age ratios to estimate X-ray and Lyα (far-UV) irradiances on K2-18b to be $F_x \sim 29 \pm 8\,\mathrm{erg\,s^{-1}\,cm^{-2}}$ and $F_{\mathrm{Ly}\alpha} \sim 61 \pm 20\,\mathrm{erg\,s^{-1}\,cm^{-2}}$. The estimated X-ray and Lyα irradiances of K2-18b are approximately 115× and 8× higher than Earth's (Guinan & Engle 2019). This indicates extensive atmospheric change through photo-evaporation (see also Van Looveren et al. 2025, Figs. 3 and 5), especially during the early evolution when the X-ray luminosity must have been even higher given the star's higher rotation rate (Johnstone et al. 2021a, hereafter CJ+21). In addition, dos Santos et al. (2020) derived the high-energy environment from *Hubble* Space Telescope (HST) Lyα observations to be $F_{\mathrm{Ly}\alpha} \sim 100.7^{+96.1}_{-82.4}\,\mathrm{erg\,s^{-1}\,cm^{-2}}$ and estimated the EUV flux of $107.9^{+124.7}_{-90.8}\,\mathrm{erg\,s^{-1}\,cm^{-2}}$ on the K2-18b following formulae for estimating EUV fluxes from Linsky et al. (2014).

Table 1. Exoplanet companions of K2-18.

Planet	M_P [$M_\oplus$]	R_P [$R_\oplus$]	a [AU]	P [days]
c^c	5.62 ± 0.84*	non-transiting	0.067	8.96
b^b	8.0 ± 1.9	2.38	0.143	32.9

Notes. ^{b}Cloutier et al. (2017); ^{c}Cloutier et al. (2019) *minimum mass ($m \sin i$).

Exoplanets around K2-18

Two transiting objects around K2-18 were initially observed with the Kepler telescope as part of the K2 mission (Montet et al. 2015) as summarized in Table 1. Later, Benneke et al. (2017) confirmed the planetary nature of the transit signal by detecting the same transit depth at a different wavelength (4.5 µm) using the Spitzer Space Telescope. The mass of K2-18b was independently determined by Cloutier et al. (2017) using the HARPS spectrograph and by Sarkis et al. (2018) with the CARMENES spectrograph. Cloutier et al. (2017) determined the mass of the K2-18b to be $8.0 \pm 1.9\,M_\oplus$. Later, the second planet, K2-18c, was confirmed with both radial-velocity instruments (Cloutier et al. 2019) as a non-transiting planet of minimum mass, $5.62 \pm 0.84\,M_\oplus \sin i$. K2-18b, with an orbital period of 33 days, has an equilibrium temperature of 272 ± 15 K (Montet et al. 2015). Figure 1 shows the orbital positions of the planets relative to the habitable zone (HZ), defined according to Kopparapu et al. (2013), where surface liquid water could exist. Kopparapu et al. (2013) described the recent Venus limit as an empirical inner boundary of the optimistic HZ. This is based on the possibility that Venus may have had liquid water until not long ago. If an exoplanet obtains no more energy from its star than Venus did during that period, it could still have conditions where surface water remains stable. A runaway greenhouse effect occurs when greenhouse gases such as $H_2O, CH_4, CO_2, N_2O,$ and O_3 trap outgoing thermal radiation, leading to rapid heating and the potential loss of surface liquid water. If water vapor reaches the stratosphere, it may escape via hydrodynamic escape, ultimately desiccating the planet (Nakajima et al. 1992). K2-18b is between the recent Venus HZ limit and the runaway greenhouse HZ limit, while K2-18c is closer to the host star.

2. Observations

The observational data used in this high-energy environment study came from eROSITA and the archives of *Chandra* and *XMM-Newton*, where K2-18 was detected adjacent to the quasar QSO B1127+078.

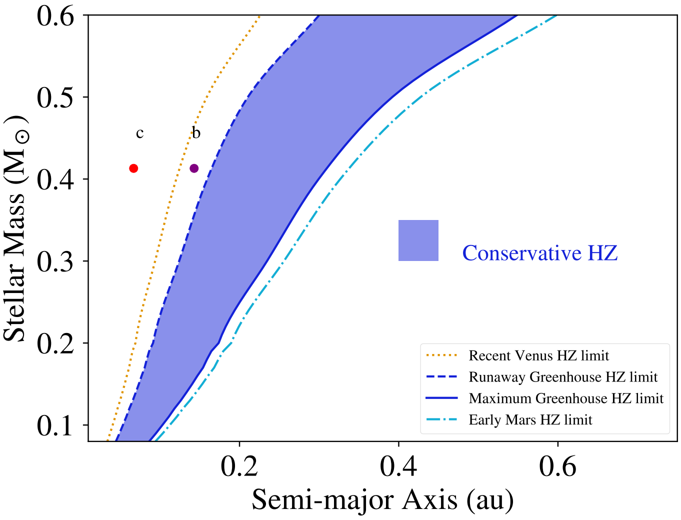

Fig. 1. Orbital positions of the K2-18 planets (colored circles) relative to the HZ are shown (Kopparapu et al. 2013). K2-18b lies near the inner edge of the conservative HZ. The dotted yellow line marks the recent Venus limit, while the region between the dash-dotted cyan line and the conservative HZ corresponds to orbital distances where water would likely remain frozen. The white regions beyond all HZ boundaries represent environments where surface liquid water is not expected to persist.

2.1. eROSITA

The extended ROentgen Survey with an Imaging Telescope Array (eROSITA) is a wide-field X-ray telescope on board the Russian-German Spectrum-Roentgen-Gamma (SRG) observatory (Predehl et al. 2021). The eROSITA observation has only provided an upper limit for this source. The data have been processed by the eSASS pipeline version 020 (Brunner et al. 2022). We report the eRASS:1 upper limit from the DR1 public release data using the upper-limit server (Tubín-Arenas et al. 2024; Merloni et al. 2024).

2.2. *Chandra*

The star K2-18 can be found in archival *Chandra* data in an ACIS-S observation targeting SDSSJ113017.37+073212.9 (PI Piconcelli, ObsID 25339). Within a total of 4 ks in December 2023, there was no detection.

2.3. *XMM-Newton*

The star K2-18 was detected during a Heritage program observation (PI: Giorgio Lanzuisi) of the quasar WISSH39 (J1130+0732). The dataset (ObsID 0943530501) includes three EPIC, 24 OM, and two RGS exposures, totalling 110 ks of observation time in December 2023. For K2-18, the data from the PN, MOS1, and MOS2 cameras are shown in Fig. 2. Each detector has a single exposure of 110 ks.

3. Methods

We describe source extraction and spectral fitting method in Sect 3.1. The model for X-ray driven evaporation of the planet atmospheres is shown in Sect 3.2.

3.1. Spectral analysis

In this work, we performed two independent spectral analyses: (1) a Bayesian inference approach; and (2) the hardness-ratio method. The data reduction was carried out using standard pipelines, specifically CIAO/Sherpa for *Chandra* data and XMM/SAS for *XMM-Newton* observations.

3.1.1. Spectral extraction

The *Chandra* data were analyzed using standard procedures from the CIAO package version 4.14 (Fruscione et al. 2006). We filtered the event list to the 0.3–10 keV energy range. Source counts were extracted using circular regions with a radius of 5″, while the background was estimated from an annular region surrounding the source. The background region has an inner radius of 10″ and an outer radius of 20″. From the *Chandra* observation, we placed an upper limit on our analysis. We proceeded consistently with the detected sources and analyzed the source spectrum and background-region spectra. The sampled posterior contains a wide range of normalizations, thus also allowing very faint source solutions that give no photons. As with the other spectra, we computed the posterior distribution of fluxes from the spectral-parameter posterior distribution. We adopted the (1σ) upper error bar of the fluxes as a flux upper limit for *Chandra*.

We processed the *XMM-Newton* PN, MOS1, and MOS2 data (see Fig. 2) following standard procedures in the *XMM-Newton* user handbook. To filter out background noise[1], we used specific selection rules for each of the EPIC detectors. We extracted a high-energy light curve using only single-pixel events (PATTERN==0) to identify intervals affected by a flaring particle background. For EPIC-MOS, the selection uses ($PI > 10\,000$), whereas for EPIC-pn it is restricted to ($10\,000 < PI < 12\,000$), with the upper bound applied to avoid the misidentification of hot pixels as very high-energy events. Good time intervals (GTIs) were generated by applying a rate threshold ($RATE \leq 0.4$ counts/s for PN and $RATE \leq 0.35$ counts/s for MOS) with `tabgtigen`, and filtered event files were created accordingly. The difference in thresholds reflects the distinct instrumental responses of MOS and PN, with PN generally exhibiting higher background levels. These GTIs were used to filter the event list, ensuring that only low-background data were retained for further analysis. The data were barycenter-corrected using `barycen`. Light curves were extracted from a 20″ circular region for the source and an annular region (60″ inner radius and 120″ outer radius) for the background using `evselect`, with energy filtering applied in the 0.2–10 keV range. Light curves were corrected for instrumental effects with `epiclccorr`. Following data reprocessing, we examined the light curves in the datasets from each *XMM-Newton* detector. The light curves showed a quasi-quiescent level of stellar activity. Figure 3 displays the *XMM-Newton* light curve showing a potential flare toward the end of the observation. As K2-18 is located close to the Solar System, we did not include a model component for ISM absorption, since it is negligible for stellar distances below 100 pc.

As our source shows relatively low counts, it is important to extract as much information as possible from the available data. This is best done by carefully modeling the spectral contribution of the background in addition to the source and analyzing

---

[1] https://www.cosmos.esa.int/web/xmm-newton/sas-thread-epic-filterbackground-in-python

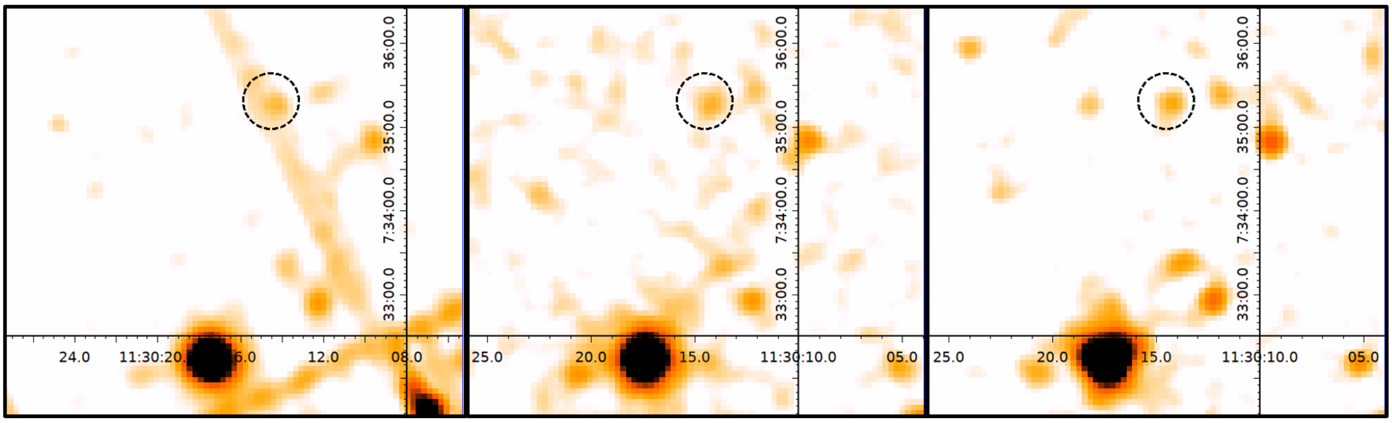

Fig. 2. K2-18 source detected on PN-CCD, MOS1, and MOS2 is marked by the dashed black circle region of 20 arcsec with its coordinates, while the dark region below corresponds to a quasar. The image is displayed with a smoothing parameter of 1.5σ. Note that the efficiency/sensitivity of MOS2 is lower than that of MOS1 (Mineo et al. 2024). In PN, the source lies in a chip gap, while it is unobstructed in MOS1 & MOS2. The X-ray flux was derived in the same way for both MOS and PN detectors.

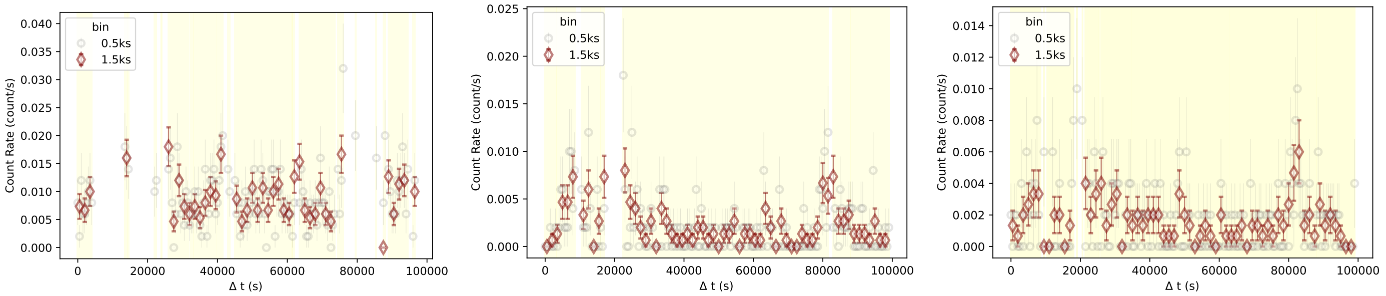

Fig. 3. K2-18 *XMM-Newton* light curves from left to right: PN, MOS1, and MOS2, showing quasi-quiescent activity. The yellow background marks the good time interval (GTI) from each detector. Two light curves are plotted with different time binnings (gray 0.5 ks bin and brown 1.5 ks bin).

with Poisson statistics (C-Stat). For the choice of the spectral model, we considered two approaches. In maximum likelihood analyses, one may use as simple a spectral model as the data require. For simplicity, we describe such an approach below, with a single-temperature plasma from the Astrophysical Plasma Emission Code (`APEC`) model (Smith et al. 2001).

An alternative is Bayesian inference, which allows us to marginalize over possible spectral models, without the need to restrict the model based on the data quality. We describe this approach here; it is presented in detail in Rukdee et al. (2024). To make Bayesian inference with X-ray spectral analysis computationally feasible, we used the spectral fitting package Bayesian X-ray Analysis, `BXA` (Buchner et al. 2014). `BXA` integrates the nested sampling algorithm `UltraNest` (Buchner 2021) with the fitting environment `CIAO/Sherpa` (Fruscione et al. 2006). To balance computational efficiency with physical accuracy, we constrained all metal abundances to a single value and modeled the plasma using ten APEC components on a logarithmic temperature grid. Normalizations follow a Gaussian profile, approximating a continuous temperature distribution. This approach captures the plasma behavior more accurately than single- or two-temperature models while remaining computationally tractable within the `BXA` framework[2]. Free parameters include peak temperature, normalization, and log-Gaussian distribution width, σ. Table 2 provides a full list of priors that control the normalization of each component. In addition, the abundance parameter sets the metal abundances of all `APEC` model components. This also includes inferred differential emission measure (DEM) distributions, which quantify the amount of plasma emitting X-rays at a given temperature and are derived by fitting the relative contributions of plasma at different temperatures to the observed spectrum. We adopted the temperature distribution outlined in Rukdee et al. (2024) to characterize the plasma behavior.

For the background-region spectrum, we adopted the background model of Simmonds et al. (2018) obtained through principal components analysis (PCA), and we fit this model to each background spectrum with BXA. Throughout our analysis, we employed Poisson (C-stat) statistics and jointly fit the source and background spectra. The background model is not a physical model, but an empirical one that is fit to the background spectrum. The background spectral fit parameters are then fixed during the analysis of the source spectrum (which includes both source and background). The empirical background model spectrum parameters are the normalizations of fixed PCA components. However, the addition is performed in log space (to ensure non-negative count rates). The PCA components for *XMM-Newton* were trained on background spectra from the *XMM-Newton* archive (Simmonds et al. 2018). Essentially, this approach approximates the extracted background spectrum with a smooth function, with a preference for creating background spectral models that resemble other *XMM-Newton* backgrounds. The background model is shown as part of the results in Sect. 4.1.

---

[2] `https://github.com/SurangkhanaRukdee/BXA-Plasma`

Table 2. Priors set for the APEC model.

Parameter	Prior	Range
abundance	uniform	0.0–1.0
kT_{peak}	log-uniform	0.1–5.0
$\mathrm{norm}_{\mathrm{peak}}$	log-uniform	10^{-6}–0.01
σ	uniform	0.0–2.0

Table 3. Relations for estimating EUV flux from Lyα for M dwarfs (M2.5 spectral type) from Linsky et al. (2014).

Wavelength Band (nm)	$\log\left[\frac{f(\Delta\lambda)}{f(\mathrm{Ly}\alpha)}\right]$
10–20	-0.491
20–30	-0.548
30–40	-0.602
40–50	$-2.294 + 0.258 \log[f(\mathrm{Ly}\alpha)]$
50–60	$-2.098 + 0.572 \log[f(\mathrm{Ly}\alpha)]$
60–70	$-1.920 + 0.240 \log[f(\mathrm{Ly}\alpha)]$
70–80	$-1.894 + 0.518 \log[f(\mathrm{Ly}\alpha)]$
80–91.2	$-1.811 + 0.764 \log[f(\mathrm{Ly}\alpha)]$
91.2–117	$-1.004 + 0.065 \log[f(\mathrm{Ly}\alpha)]$

We independently confirmed the results of the Bayesian analysis that we present in Sect. 4 using a more traditional spectral analysis with Xspec for the extracted CCD spectra from MOS1 and MOS2; i.e., the detectors where the source was not located on a chip edge, with similar outcomes for the coronal temperature and stellar X-ray fluxes. Furthermore, we confirmed the overall coronal temperature reported in Sect. 4, with a hardness-ratio analysis similar to that of Ilic et al. (2022); i.e., we calculated the hardness ratio of the star with 0.2–0.7 keV as the soft band and 0.7–2.0 keV as the hard band and compared this to expected hardness ratios for single-temperature coronal models, again with comparable results to those of the Bayesian analysis.

The upper limit of the background flux was computed in the 0.6–2.3 keV band for *Chandra*, while the X-ray flux was computed in the 0.2–2.0 keV band for *XMM-Newton*. For the flux conversion, we converted the HST Lyα to EUV flux using the method from Linsky et al. (2014) for an M2.5 star, applying the conversion factors listed in Table 3 and summing over all bands from 10 to 117 nm. For the EUV-to-X-ray relation, we adopted the Sanz-Forcada et al. (2011, hereafter SF+11) relation. In SF+11, the EUV flux was calculated by generating a synthetic spectrum using a coronal model based on the emission-measure distribution, coronal abundances, and the Astrophysics Plasma Emission Database (APED; Smith et al. 2001).

3.2. Modeling stellar and planetary evolution

For the stellar evolutionary model linked to atmospheric escape, we explored an approach using the hydrodynamic model with energy-limited escape, implemented via the `VPLanet` framework (Barnes et al. 2020). The results are also put into context with Jeans' escape calculations of Earth's early evolution (Johnstone et al. 2021b). These models provide context for our discussion and help interpret the observational data. Salz et al. (2016) and Krenn et al. (2021) performed a critical assessment of the applicability of the energy-limited approximation (Watson et al. 1981) for estimating exoplanetary mass-loss rates by comparing it to a grid of hydrodynamic models computed by Kubyshkina et al. (2018). They concluded that the energy-limited approximation can be used as an order-of-magnitude estimate for planets with intermediate gravitational potentials and low-to-intermediate equilibrium temperatures (300 K–2000 K) and XUV irradiation levels. However, the XUV irradiation level depends on the evolution of the stellar rotation period of the host star, which is non-unique for a 0.4 solar mass star up to 2 Gyr (Van Looveren et al. 2025). We note that the work of Van Looveren et al. (2025) focuses on atmospheres dominated by CO_2 and N_2, whereas K2-18b is currently believed to host an H_2-rich atmosphere. Furthermore, the planet's higher mass enhances atmospheric retention by making it more difficult for gases to escape compared to a lower-mass planet.

We used the Model for Rotation of Stars (`MORS`)[3] from CJ+21 to describe the stellar evolution. It provides a comprehensive rotation–L_X–EUV–age framework spanning the full main-sequence evolution of cool stars, including non-unique pathways before 1 Gyr. It models different scenarios of evolutionary tracks depending on the rotation-rate percentile, with the three scenarios "slow", "medium", and "fast", corresponding to the 5th, 50th, and 95th percentiles of the rotation distribution. For this model, Johnstone et al. (2021b) examined the minimum CO_2 levels required to retain an atmosphere under high XUV flux, focusing on young stars and early Earth-like conditions. Later, Van Looveren et al. (2025) introduced the atmosphere retention distance for Earth-sized planets in stellar HZs, combining thermochemical and stellar evolution models. Their analysis accounts for stellar rotation rates and associated XUV output to assess where CO_2- or N_2-dominated atmospheres can be retained across a range of stellar masses.

Energy-limited mass loss

Next, we investigated the host star's role in planetary mass loss. We determined the mass-loss rate with the energy-limited model (Lopez et al. 2012; Owen & Jackson 2012) using the following equation:

$$\dot{M} = \epsilon \times \frac{\pi R_{\mathrm{XUV}}^2 F_{\mathrm{XUV}}}{K G M_{\mathrm{pl}} / R_{\mathrm{pl}}}, \quad (1)$$

where $\dot{M}$ is the mass-loss rate, ϵ the efficiency factor from atmospheric escape assumed to be 0.15 (Foster et al. 2022), R_{XUV} the planetary radius in XUV wavelength adopted to be 1.1 times the planetary radius in optical, M_{pl} the planetary mass, K a factor indicating the effect of Roche-lobe overflow set to 1, G the gravitational constant, and F_{XUV} the sum of the observed X-ray and estimated EUV fluxes of the host star. Here, we derived the EUV luminosity from the X-ray luminosity following Eq. (3) in SF+11.

The efficiency factor, ϵ, measures the fraction of incoming stellar XUV energy that is converted to drive atmospheric escape. For hydrogen–helium atmospheres, ϵ is usually modeled on the order of 10 to 30% (see, e.g., Lammer 2013, Owen & Wu 2013, Salz et al. 2016, Poppenhaeger et al. 2024). This range is based on early hydrodynamic simulations showing that a significant fraction of the absorbed energy is radiated away since much of the absorbed energy is lost to radiative cooling, mainly through Lyman-α emission (Salz et al. 2015). These values,

---

[3] `https://github.com/ColinPhilipJohnstone/Mors`

however, come almost entirely from hydrogen-dominated models (Watson et al. 1981), from which heavier species such as C, N, and O are not expected to escape. For atmospheres enriched in heavier molecules, a large share of the XUV input may instead drive photochemistry, leaving even less energy available for escape. This makes ϵ highly uncertain for mixed or metal-rich envelopes such as that of K2-18b. Even for pure H/He atmospheres, hydrodynamic simulations (Krenn et al. 2021) show that energy-limited estimates do not reliably match mass-loss rates in any regime, and the uncertainties remain large. For these reasons, we used the energy-limited expression only as a qualitative diagnostic and under the assumption of a hydrogen-only atmosphere, with ϵ remaining a major and unresolved source of uncertainty in atmospheric escape estimates for sub-Neptune planets. When applying the energy-limited formula, we adopted a conservative efficiency factor of 0.15. This is within the range well supported by detailed simulations in the literature (Shematovich et al. 2014).

We calculated the XUV flux received by the planet ($F_{\rm pl,xuv}$) by dividing the total stellar XUV luminosity ($L_{\rm tot,xuv}$) by the surface area of a sphere with a radius equal to the planet's orbital distance (a), $F_{\rm pl} = L_{\rm total}/(4\pi a^2)$. The resulting flux is expressed in units of erg s^{-1} cm^{-2}.

In addition to Eq. (1), we used the `VPLanet` suite to provide an overview of planetary evolution. Due to limitations in the mini-Neptune radius model embedded in `VPLanet`, we describe the method and present the results in Appendix A.

4. Results

In this section, we present the results from the analysis of X-ray observations obtained from *Chandra* and *XMM-Newton*. These observations provided X-ray properties and the activity levels of K2-18. Additionally, we report the upper-limit value from eROSITA observations according to eROSITA Data Release 1 from the upper limit server (Tubín-Arenas et al. 2024; Merloni et al. 2024).

4.1. X-ray properties from spectral analysis

The spectral fits and parameter constraints from `BXA` for the *XMM-Newton* data, with a GTI duration of 57166.05 s, 91064.42, and 95408.17 for PN, MOS,1 and MOS2 respectively, are shown in Fig. 4.

The inferred DEM distributions, computed with `APEC`, are presented in Fig. 5 for the reconstructed continuous DEM, with the average distribution shown as a solid black line. For the *XMM-Newton* observation, the DEM is poorly constrained due to the low counts. We obtained the best statistical constraints for the DEM from MOS1, which is shown in Fig. 5. The peak temperature ($kT_{\rm peak}$) and the width of the distribution (kT_{σ}) from all detectors are listed in Table 4. The abundance was not tightly constrained, but approximately 0.15 solar in PN and MOS2, which is not ruled out by the constraints of MOS1. The focus of this work is however on the X-ray flux, which the low counts clearly constrain to a notably low value. We calculated the X-ray flux of $4.13^{+1.12}_{-0.98} \times 10^{-15}$ erg s^{-1} cm^{2} from MOS1. We obtained comparable X-ray fluxes of $5.89^{+1.04}_{-0.96}$ erg s^{-1} cm^{2} and $4.36^{+0.97}_{-0.97}$ erg s^{-1} cm^{2} for PN and MOS2, respectively. The differences between the PN and MOS results are minimal: on the order of ~0.15 dex in log $L_{\rm X}$. From the *Chandra* observation, we set a 1σ upper limit of <9.09×10^{-15} erg s^{-1} cm^{2}.

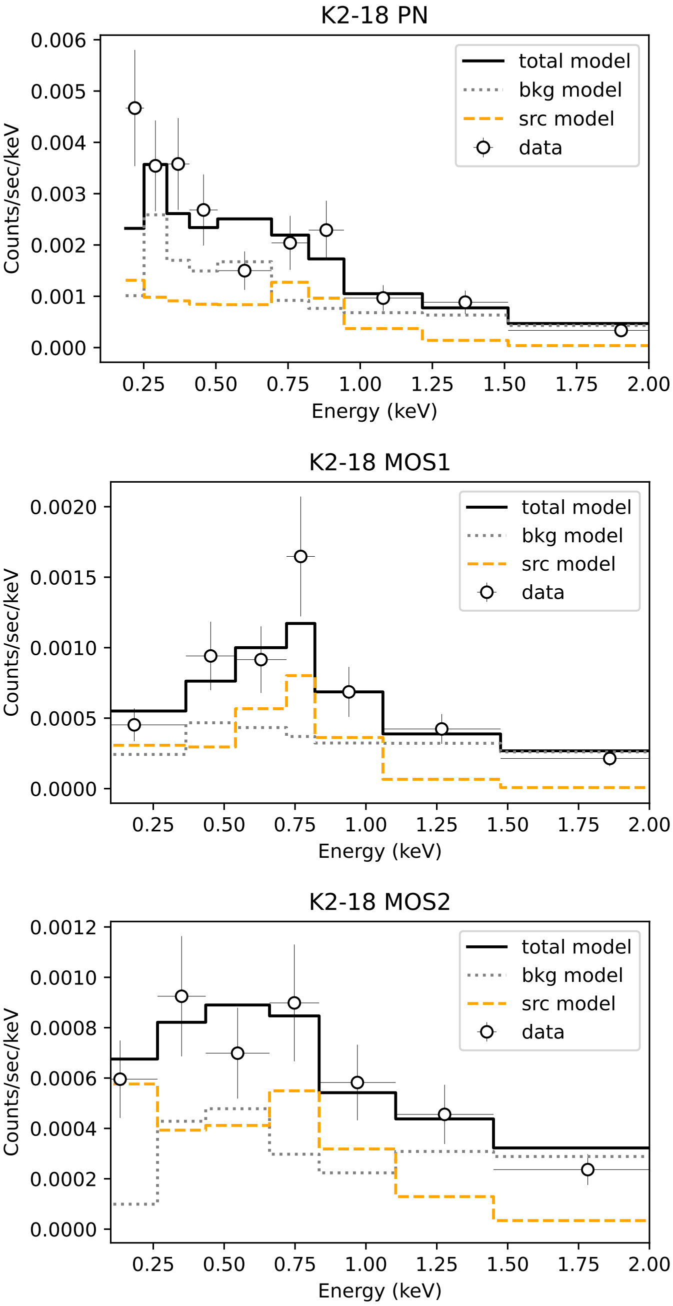

Fig. 4. X-ray spectrum of K2-18 analyzed over the 0.2–2.0 keV range, extracted from the PN-CCD (top), MOS1 (middle), and MOS2 (bottom) on *XMM-Newton* during a 100 ks observation. The solid black line is the spectral model through `BXA-Plasma`, the dashed orange line is the source model, and the dotted gray line is the background model with PCA routine in `BXA`.

4.2. X-ray and UV context

The light curve of the X-ray flux over time from various missions over approximately four years is presented in Fig. 6. Before the X-ray observations, the star K2-18 was observed during two transits on June 18, 2017 and March 9, 2018 (Program GO-14221, PI: D. Ehrenreich) using HST/STIS and the grating G140M (resolving power $R \sim 10\,000$). The HST Lyα flux was taken from Fig. 3 of dos Santos et al. (2020), using the average value of data points to represent the stellar environment. We selected the red wing of the Lyα line, before the transit, which

Table 4. Soft X-ray flux properties for K2-18 across different observations.

Date	Observatory	Duration [ks]	Flux [10^{-15} erg cm^{-2} s^{-1}]	logLx [erg/s]	$L_x/L_{\rm bol}$ [10^{-5}]	$kT_{\rm peak}$ [keV]	kT_σ [keV]	Abundance [Solar]
2020	eROSITA	6.20	<140.73	<28.38		–	–	–
2023-12	*Chandra*	40.0	< 9.09	<27.20		–	–	–
2024-12	XMM PN*	110.0	$5.89^{+1.04}_{-0.96}$	27.01 ± 0.08	1.33 ± 0.23	0.51 ± 0.72	0.86 ± 0.48	0.15 ± 0.12
2024-12	XMM MOS1	110.0	$4.13^{+1.12}_{-0.98}$	26.85 ± 0.11	0.93 ± 0.24	0.35 ± 0.15	0.28 ± 0.26	0.46 ± 0.24
2024-12	XMM MOS2	110.0	$4.36^{+0.97}_{-0.97}$	26.88 ± 0.10	0.98 ± 0.22	0.42 ± 0.50	0.63 ± 0.42	0.18 ± 0.17

Notes. *Flux calculated for energy band 0.2–2.0 keV for *XMM Newton*.

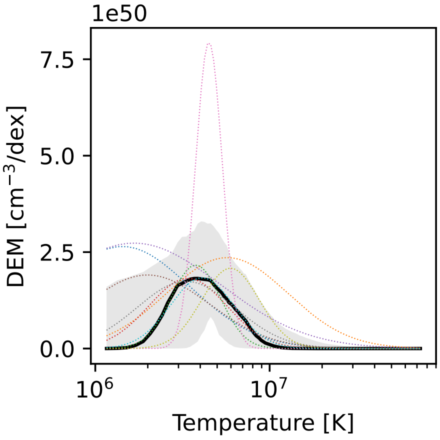

Fig. 5. Reconstructed continuous DEM distribution from MOS1. The black curve shows the median of the posterior DEM predictions, and the gray band contains 68% of the distribution. The colorful dotted lines are ten random posterior samples of possible DEM distributions. Note that the kT values from PN and MOS2 are not well constrained and are not shown here.

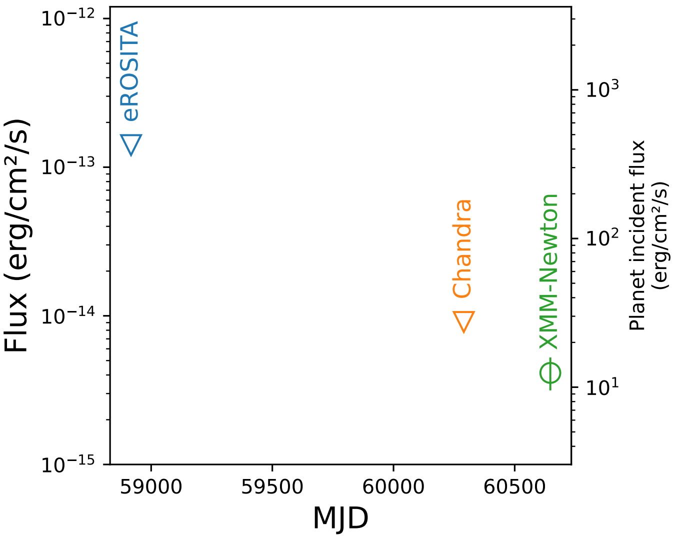

Fig. 6. Light curve of the high-energy X-ray flux over four years comprising the upper limit from eROSITA and *Chandra* and the *XMM-Newton* measurement.

appears more stable and better constrained, and find a Lyα flux of $0.78^{+0.19}_{-0.16} \times 10^{-15}$ erg cm^{-2} s^{-1} for the first visit (Visit A) and $1.81^{+0.23}_{-0.23} \times 10^{-15}$ erg cm^{-2} s^{-1} for the second visit (Visit B). Lyα flux serves as a proxy for the total FUV flux, accounting for approximately 75% to 90% of the FUV emission in M dwarfs Guinan & Engle (2019). We did not include the EUV flux converted to X-ray in Fig. 6 as it was found to be unrealistically low.

In this work, the *XMM-Newton* detection provides a tight and direct constraint on the X-ray flux. Results from our Bayesian method (Fig. 4 and Fig. 5) are consistent with a flux of $3.70^{+0.74}_{-0.69} \times 10^{-15}$erg s^{-1} cm^{-2} derived from the simpler hardness-ratio method, corresponding to an X-ray luminosity of $\sim 7 \times 10^{26}$ erg s^{-1}. The ratio, $L_{\rm XUV}/L_{\rm bol} \sim 10^{-5}$, indicates a low present-day stellar activity level.

We estimated the stellar EUV luminosity ($L_{\rm EUV}$) from Ly-α flux from HST visit B reported by dos Santos et al. (2020) using the Linsky et al. (2014) relation (range 10-117 nm) to be 2.7×10^{26} erg s^{-1} and combined it with our X-ray measurement resulting in XUV luminosity of 9.78×10^{26} erg s^{-1}. The corresponding XUV flux received by K2-18b is $\sim$17.03 erg s^{-1} cm^{-2}.

For an instantaneous estimation based on energy-limited escape of the atmosphere, we calculated an atmospheric mass-loss rate driven by XUV radiation from Eq. (1) to be 1.07×10^7 g s^{-1}, which is an order of magnitude less than the total escape rate of 10^8 g s^{-1} previously reported by dos Santos et al. (2020) from the HST measurement. This is further illustrated in the planetary evolution model from VPLanet (Barnes et al. 2020), shown in Fig. A.1, where the planetary mass and radius exhibit minimal change over a billion-year timescale.

The measured value from the MOS1 observation is placed onto Fig. 7, which shows the stellar evolution track from CJ+21 appropriate for K2-18 ($M_* = 0.41\,M_\odot$, Prot = 38.6 days at present). We find that the Lehmer & Catling (2017) model of mini-Neptune has a maximum planet radius limitation at 2.2 $R_\oplus$ shown in Fig. A.1. Alternatively, we do not apply the planet model and instead leave the radius fixed at the present-day measured planet radius of 2.38 $R_\oplus$. The resulting envelope mass-loss rate is $6.2 \times 10^{-7}\,M_\oplus\,{\rm Myr}^{-1}$ from `VPLanet`, whereas with the energy-limited mass-loss calculation (Eq. (1)) using the present-day flux yields $5.63 \times 10^{-8}\,M_\oplus\,{\rm Myr}^{-1}$, which is about an order of magnitude lower than what the model predicted. Here, we again see a discrepancy in the mass-loss rate that may be related to the similarly large discrepancy between the modeled and the observed X-ray luminosities in Fig. 7.

5. Discussion

We investigated if the observed level of XUV flux is sufficiently low to allow atmospheric retention. Current observations suggest that K2-18b possesses an atmosphere. Interior structure

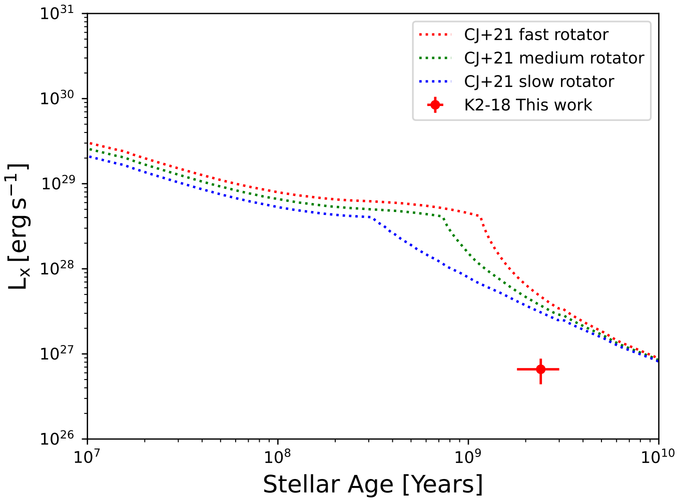

Fig. 7. Stellar evolutionary track of X-ray luminosity from Johnstone et al. (2021a, CJ+21). The age of K2-18 is adopted from Guinan & Engle (2019). The dotted lines show the evolution track generated with `MORS` for different percentiles of the rotation distribution: (red) fast rotator, (green) medium rotator, and (blue) slow rotator. The measured X-ray luminosity is almost an order of magnitude lower than the expectation from the model.

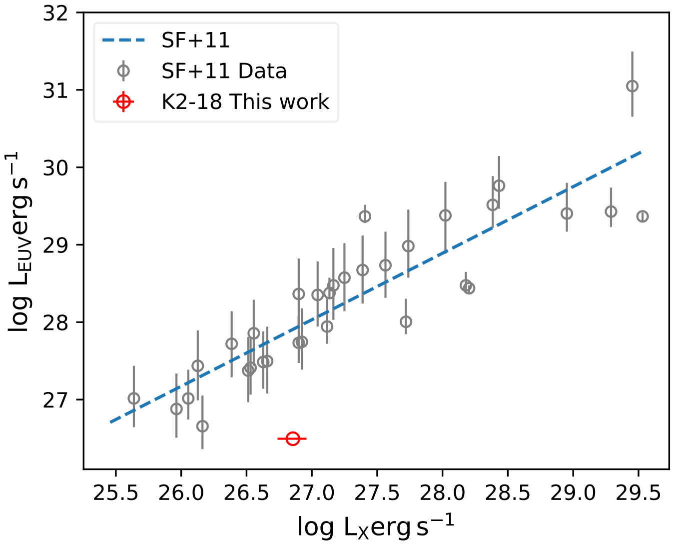

Fig. 8. X-ray and UV luminosity of the K2-18 system, with Lyα emission representing the EUV flux and *XMM-Newton* observations. The X-ray flux plotted against the empirical relation derived from sample (gray data points) from SF+11. The red point is given by its observed *XMM-Newton* X-ray luminosity and by the EUV luminosity inferred from with Lyα from dos Santos et al. (2020).

models indicate that planets in this size range likely have a solid or rocky core enveloped by a thick, hydrogen-rich atmosphere (Cloutier et al. 2017), with volatiles such as water potentially surrounding the core (Tsiaras et al. 2019).

In this work, we presented the observed X-ray flux of the system K2-18. In the context of stellar activity, the surface X-ray flux of low-mass stars, particularly M dwarfs, spans a wide range, reflecting their magnetic activity levels (Caramazza et al. 2023). Low X-ray emission of such stars is often consistent with other indicators–such as low metallicity and slow rotation, suggesting an old age and a quiescent magnetic environment. Unlike previous assumptions of a constant L_X level in the saturated regime, Magaudda et al. (2020) showed that L_X decreases slightly with increasing $P_{\rm rot}$, that the saturated L_X level decreases with lower stellar mass, and that the transition point ($P_{\rm rot,sat}$) shifts to longer periods for lower mass stars. The L_X–$P_{\rm rot}$ relation for K2-18's stellar mass and rotation period places the system in the unsaturated regime, with an expected $\log L_X \sim 27$ erg s^{-1}.

Previous observations by dos Santos et al. (2020) using Lyα transit spectroscopy provided evidence of hydrogen escape from K2-18b's atmosphere, which is likely driven by EUV radiation. Their study estimated an EUV irradiation level of 10^1–10^2 erg s^{-1} cm^{-2} using the energy-limited escape from Salz et al. (2015) corresponding to a loss of the planet's mass over its lifetime of less than 1%, while allowing it to maintain a volatile-rich atmosphere. dos Santos et al. (2020) concluded that K2-18b possesses an H-rich atmosphere. We included the Lyα flux measurement from dos Santos et al. (2020), converted it to EUV using the relation from Linsky et al. (2014) –along with the X-ray measurement from this work– and found that K2-18 lies an order of magnitude below the SF+11 relation. This is shown in Fig. 8. With an energy-limited escape model over the evolution of the star, we also find that K2-18b can retain its atmosphere (see Appendix A).

Previous observations by Montet et al. (2015) estimated the equilibrium temperature of K2-18b – derived from the star's bolometric luminosity – to be similar to Earth's average surface temperature of approximately 288 K. According to the present-day measured rotation and stellar mass, K2-18 should have fallen onto the fast rotator track. However, the measured X-ray luminosity of the system is lower than expected for a 0.4 $M_\odot$ star with a rotation period of 38.6 days. Previous findings from ground-based observations suggest that low-activity M dwarfs are more common among older, less massive stars with reduced magnetic activity (Houdebine et al. 2012; Robertson et al. 2013; Maldonado et al. 2017).

The incident flux on the planet and its effect on the temperature profile or thermal structure have been studied using various models. Intense XUV radiation leads to heating of the upper atmosphere, causing it to expand and form extended exospheres (Lammer et al. 2007), while carbon-bearing species such as CO_2 affect the cooling process (Johnstone et al. 2021b). General circulation models show that stellar irradiation also influences large-scale atmospheric dynamics, including circulation patterns, cloud formation, and observable properties such as phase curves and albedo. For super-Earths with rocky cores and secondary atmospheres, retention depends on factors such as atmospheric composition, stellar mass, and stellar evolution. Van Looveren et al. (2025) demonstrated that for a ~1 Earth-mass planet, the host star's XUV flux and activity history play a key role in determining long-term atmospheric survival.

Figure 1 shows that the planet resides between the recent Venus and runaway greenhouse HZ limits. Observations showing the presence of CH_4 in K2-18b's atmosphere possibly indicate an ongoing runaway greenhouse effect, which is strengthened by the thermal structure context in Fig. 9. Here, we placed observational constraints on the model from Johnstone et al. (2021b), where the measurement of the CO_2 mixing ratio of $10^{(-1.75^{+0.45}_{-1.03})}$ is taken from the no-offset results of Madhusudhan et al. (2023). The no-offset case refers to the baseline scenario where the NIRISS and NIRSpec spectra are combined directly, without introducing any relative flux adjustments between the instruments or channels. However, if K2-18b

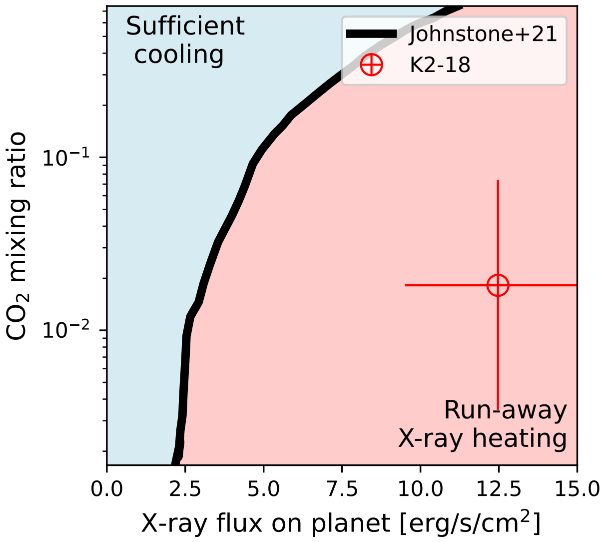

Fig. 9. Thermal structure relation of CO_2 (cooling process) and X-ray flux (heating process) on the planet, adapted from Johnstone et al. (2021b). The overlaid boundary (solid black line) corresponds to a CO_2- and N_2-dominated atmosphere, while K2-18b is expected to be H/He-rich with CO_2 as a minor species. The X-ray flux is measured in this work, and the CO_2 mixing ratio is taken from Madhusudhan et al. (2023, no offset).

is hydrogen-rich, then H_3^+ would play a more significant role in cooling the atmosphere (Miller et al. 2010), while CO_2 would have little influence on the cooling process. The X-ray flux on the planet of $F_{\mathrm{pl},x} = 12.47^{+3.38}_{-2.96}\,\mathrm{erg\,s^{-1}\,cm^{-2}}$ is from *XMM-Newton* MOS1 (this work). In Fig. 9, the overlaid model curve of Johnstone et al. (2021b) describes the balance between cooling, driven by carbon-bearing species such as CO_2, and heating from the high-energy flux incident on the planet. At face value, our X-ray measurement (red error bar in Fig. 9) implies that there is not enough CO_2 to prevent runaway X-ray heating in K2-18b. We note that this model assumes a CO_2- and N_2-dominated atmosphere, whereas K2-18b is expected to be H/He-rich with CO_2 only being a minor species. In addition, Turbet et al. (2019) showed that planets undergoing runaway greenhouse evolution develop thick, water-vapor-dominated atmospheres, significantly inflating their radii –an effect that is observable from space missions. For a better understanding of diverse exoplanetary thermal structures, further observations of sub-Neptunes are essential to place stronger constraints on this model.

Our team, under the Methane Atmospheres Related to Stellar Hosts (MARSH) collaboration, is conducting observations with *XMM-Newton* and VLT/CRIRES+ to constrain thermal structure models following the frameworks of Johnstone et al. (2021b) and Van Looveren et al. (2025). These efforts aim to better our understanding of the relevant conditions by populating the parameter space shown in Fig. 9 and refining the models for different stellar types, which should also be considered. Looking ahead, future instruments such as ANDES on the ELT aim to characterize non-transiting temperate rocky exoplanets around nearby M dwarfs, including Proxima Centauri b and Barnard's Star b. These targets form a "golden sample" (Palle et al. 2025) of nearby potentially habitable worlds accessible for detailed atmospheric studies.

6. Conclusions

This study investigated, from a stellar perspective, why K2-18b appears capable of retaining its atmosphere despite orbiting an M-dwarf star in close proximity to its host. The high-energy radiation environment of exoplanets plays a crucial role in shaping atmospheric escape, chemical evolution, and potential habitability. By combining X-ray and EUV observations with atmospheric spectroscopy, we can begin to map star–planet interactions and understand how stellar activity influences exoplanetary atmospheres over time. We find that K2-18 is relatively inactive, as evidenced by its low X-ray luminosity, although small flares are observed. Its activity level (Lx/Lbol) is an order of magnitude higher than that of the present-day Sun. This activity range (Lx/Lbol is 0.93-1.33 $\times 10^{-5}$) of the host star may represent a sweet spot for future atmospheric characterization–active enough to drive detectable atmospheric signals, yet not so extreme as to cause rapid atmospheric erosion.

The star K2-18's X-ray-flux measurement provides essential constraints for atmospheric escape and planetary photochemical modeling. The host stars of the most promising habitable planets may be similarly quiet. To accurately characterize the spectra of such quiet stars, reasonable exposure times and instruments with higher effective areas are required. The upcoming NewAthena (Cruise et al. 2025) mission, with its increased telescope effective area and WFI camera (Rau et al. 2013) will be essential for advancing studies of exoplanetary high-energy environments.

Acknowledgements. SR thanks Vinay Kashyap and Nick Durham for a discussion regarding the *Chandra* calibration. KP and IV acknowledge support from the European Research Council (ERC) under grant agreement 101170037 (Evaporator). JVS and GR acknowledge support by the Munich Institute for Astro-, Particle and BioPhysics (MIAPbP) which is funded by the Deutsche Forschungsgemeinschaft (DFG, German Research Foundation) under Germany´s Excellence Strategy – EXC-2094 – 390783311. We thank the anonymous referee for their constructive comments, which have helped improve this manuscript. This work is based on data from eROSITA, the soft X-ray instrument aboard SRG, a joint Russian-German science mission supported by the Russian Space Agency (Roskosmos), in the interests of the Russian Academy of Sciences represented by its Space Research Institute (IKI), and the Deutsches Zentrum für Luft- und Raumfahrt (DLR). The SRG spacecraft was built by Lavochkin Association (NPOL) and its subcontractors, and is operated by NPOL with support from the Max Planck Institute for Extraterrestrial Physics (MPE). The development and construction of the eROSITA X-ray instrument was led by MPE, with contributions from the Dr. Karl Remeis Observatory Bamberg & ECAP (FAU Erlangen-Nuernberg), the University of Hamburg Observatory, the Leibniz Institute for Astrophysics Potsdam (AIP), and the Institute for Astronomy and Astrophysics of the University of Tübingen, with the support of DLR and the Max Planck Society. The Argelander Institute for Astronomy of the University of Bonn and the Ludwig Maximilians Universität Munich also participated in the science preparation for eROSITA. The eROSITA data shown here were processed using the eSASS/NRTA software system developed by the German eROSITA consortium.

References

Amaral, L. N. R. d., Shkolnik, E. L., Loyd, R. O. P., & Peacock, S. 2025, ApJ, 985, 100
Audard, M., Güdel, M., Drake, J. J., & Kashyap, V. L. 2000, ApJ, 541, 396
Aulanier, G., Démoulin, P., Schrijver, C. J., et al. 2013, A&A, 549, A66
Baraffe, I., Homeier, D., Allard, F., & Chabrier, G. 2015, A&A, 577, A42
Barnes, R., Luger, R., Deitrick, R., et al. 2020, PASP, 132, 024502
Becker, J., Gallo, E., Hodges-Kluck, E., Adams, F. C., & Barnes, R. 2020, AJ, 159, 275
Benneke, B., Werner, M., Petigura, E., et al. 2017, ApJ, 834, 187
Benneke, B., Wong, I., Piaulet, C., et al. 2019, ApJ, 887, L14
Benneke, B., Roy, P. A., Coulombe, L. P., et al. 2024, arXiv e-prints [arXiv:2403.03325]
Brunner, H., Liu, T., Lamer, G., et al. 2022, A&A, 661, A1
Buchner, J. 2021, J. Open Source Software, 6, 3001
Buchner, J., Georgakakis, A., Nandra, K., et al. 2014, A&A, 564, A125

Cadieux, C., Doyon, R., MacDonald, R. J., et al. 2024, ApJ, 970, L2
Caramazza, M., Stelzer, B., Magaudda, E., et al. 2023, A&A, 676, A14
Cloutier, R., Astudillo-Defru, N., Doyon, R., et al. 2017, A&A, 608, A35
Cloutier, R., Astudillo-Defru, N., Doyon, R., et al. 2019, A&A, 621, A49
Cohen, O., & Drake, J. J. 2014, ApJ, 783, 55
Cooke, G. J., & Madhusudhan, N. 2024, ApJ, 977, 209
Cruise, M., Guainazzi, M., Aird, J., et al. 2025, Nat. Astron., 9, 36
Davenport, J. R. A. 2016, ApJ, 829, 23
Davenport, J. R. A., Covey, K. R., Clarke, R. W., et al. 2019, ApJ, 871, 241
do Amaral, L. N. R., Barnes, R., Segura, A., & Luger, R. 2022, ApJ, 928, 12
dos Santos, L. A., Ehrenreich, D., Bourrier, V., et al. 2020, A&A, 634, L4
Dressing, C. D., & Charbonneau, D. 2013, ApJ, 767, 95
Ehrenreich, D., & Désert, J. M. 2011, A&A, 529, A136
Foster, G., Poppenhaeger, K., Ilic, N., & Schwope, A. 2022, A&A, 661, A23
France, K., Froning, C. S., Linsky, J. L., et al. 2013, ApJ, 763, 149
France, K., Loyd, R. O. P., Youngblood, A., et al. 2016, ApJ, 820, 89
Fromont, E. F., Ahlers, J. P., do Amaral, L. N. R., et al. 2024, ApJ, 961, 115
Fruscione, A., McDowell, J. C., Allen, G. E., et al. 2006, in Society of Photo-Optical Instrumentation Engineers (SPIE) Conference Series, eds. D. R. Silva, &R. E. Doxsey, SPIE Conf. Ser., 6270, 62701V
Fulton, B. J., & Petigura, E. A. 2018, AJ, 156, 264
Fulton, B. J., Petigura, E. A., Howard, A. W., et al. 2017, AJ, 154, 109
Greene, T. P., Bell, T. J., Ducrot, E., et al. 2023, Nature, 618, 39
Gronoff, G., Arras, P., Baraka, S., et al. 2020, J. Geophys. Res. (Space Phys.), 125, e27639
Güdel, M., Audard, M., Skinner, S. L., & Horvath, M. I. 2002, ApJ, 580, L73
Guinan, E. F., & Engle, S. G. 2019, Res. Notes AAS, 3, 189
Günther, M. N., Zhan, Z., Seager, S., et al. 2020, AJ, 159, 60
Gupta, A., Stixrude, L., & Schlichting, H. E. 2025, ApJ, 982, L35
Hawley, S. L., Davenport, J. R. A., Kowalski, A. F., et al. 2014, ApJ, 797, 121
Heath, M. J., Doyle, L. R., Joshi, M. M., & Haberle, R. M. 1999, Origins Life Evol. Biosphere, 29, 405
Hejazi, N., Crossfield, I. J. M., Souto, D., et al. 2024, ApJ, 973, 31
Houdebine, E. R., Butler, C. J., Garcia-Alvarez, D., & Telting, J. 2012, MNRAS, 426, 1591
Howard, A. W., Marcy, G. W., Bryson, S. T., et al. 2012, ApJS, 201, 15
Hu,, R., Bello-Arufe, A., Tokadjian, A., et al. 2025, arXiv e-prints [arXiv:2507.12622]
Hu, R., Damiano, M., Scheucher, M., et al. 2021, ApJ, 921, L8
Huang, Z., Yu, X., Tsai, S.-M., et al. 2024, ApJ, 975, 146
Ilic, N., Poppenhaeger, K., & Hosseini, S. M. 2022, MNRAS, 513, 4380
Johnstone, C. P., Güdel, M., Lammer, H., & Kislyakova, K. G. 2018, A&A, 617, A107
Johnstone, C. P., Bartel, M., & Güdel, M. 2021a, A&A, 649, A96
Johnstone, C. P., Lammer, H., Kislyakova, K. G., Scherf, M., & Güdel, M. 2021b, Earth Planet. Sci. Lett., 576, 117197
Ketzer, L., & Poppenhaeger, K. 2023, MNRAS, 518, 1683
Kopparapu, R. K., Ramirez, R., Kasting, J. F., et al. 2013, ApJ, 765, 131
Krenn, A. F., Fossati, L., Kubyshkina, D., & Lammer, H. 2021, A&A, 650, A94
Kubyshkina, D., Fossati, L., Erkaev, N. V., et al. 2018, ApJ, 866, L18
Lammer, H. 2013, Origin and Evolution of Planetary Atmospheres
Lammer, H., Selsis, F., Ribas, I., et al. 2003, ApJ, 598, L121
Lammer, H., Lichtenegger, H. I., Kulikov, Y. N., et al. 2007, Astrobiology, 7, 185
Lammer, H., Bredehöft, J. H., Coustenis, A., et al. 2009, A&A Rev., 17, 181
Lehmer, O. R., & Catling, D. C. 2017, ApJ, 845, 130
Lin, R. P. 1994, EOS Trans., 75, 457
Linsky, J. L., Fontenla, J., & France, K. 2014, ApJ, 780, 61
Lopez, E. D., & Fortney, J. J. 2013, ApJ, 776, 2
Lopez, E. D., Fortney, J. J., & Miller, N. 2012, ApJ, 761, 59
Loyd, R. O. P., France, K., Youngblood, A., et al. 2018, ApJ, 867, 71
Luque, R., Piaulet-Ghorayeb, C., Radica, M., et al. 2025, A&A, 700, A284
Luu, C. N., Yu, X., Glein, C. R., et al. 2024, ApJ, 977, L51
Madhusudhan, N., Nixon, M. C., Welbanks, L., Piette, A. A. A., & Booth, R. A. 2020, ApJ, 891, L7
Madhusudhan, N., Piette, A. A. A., & Constantinou, S. 2021, ApJ, 918, 1
Madhusudhan, N., Sarkar, S., Constantinou, S., et al. 2023, ApJ, 956, L13
Madhusudhan, N., Constantinou, S., Holmberg, M., et al. 2025, ApJ, 983, L40
Magaudda, E., Stelzer, B., Covey, K. R., et al. 2020, A&A, 638, A20
Maggio, A., Pillitteri, I., Argiroffi, C., et al. 2023, ApJ, 951, 18
Maldonado, J., Scandariato, G., Stelzer, B., et al. 2017, A&A, 598, A27
Matt, S. P., MacGregor, K. B., Pinsonneault, M. H., & Greene, T. P. 2012, ApJ, 754, L26
Matt, S. P., Brun, A. S., Baraffe, I., Bouvier, J., & Chabrier, G. 2015, ApJ, 799, L23
McCreery, P., Dos Santos, L. A., Espinoza, N., Allart, R., & Kirk, J. 2025, ApJ, 980, 125
Meadows, V. S., Arney, G. N., Schwieterman, E. W., et al. 2018, Astrobiology, 18, 133
Merloni, A., Lamer, G., Liu, T., et al. 2024, A&A, 682, A34
Miller, S., Stallard, T., Melin, H., & Tennyson, J. 2010, Faraday Discuss., 147, 283
Mineo, T., Fioretti, V., Lotti, S., et al. 2024, A&A, 691, A230
Montet, B. T., Morton, T. D., Foreman-Mackey, D., et al. 2015, ApJ, 809, 25
Nakajima, S., Hayashi, Y.-Y., & Abe, Y. 1992, J. Atmos. Sci., 49, 2256
Owen, J. E., & Jackson, A. P. 2012, MNRAS, 425, 2931
Owen, J. E., & Wu, Y. 2013, ApJ, 775, 105
Palle, E., Biazzo, K., Bolmont, E., et al. 2025, Exp. Astron., 59, 29
Pica-Ciamarra, L., Madhusudhan, N., Cooke, G.J., Constantinou, S., & Binet, M. 2025, arXiv e-prints [arXiv:2505.10539]
Piette, A. A. A., & Madhusudhan, N. 2020, ApJ, 904, 154
Poppenhaeger, K., Ketzer, L., & Mallonn, M. 2021, MNRAS, 500, 4560
Poppenhaeger, K., Ketzer, L., Ilic, N., et al. 2024, A&A, 689, A188
Predehl, P., Andritschke, R., Arefiev, V., et al. 2021, A&A, 647, A1
Ramirez, R. M., & Kaltenegger, L. 2014, ApJ, 797, L25
Rau, A., Meidinger, N., Nandra, K., et al. 2013, arXiv e-prints [arXiv:1308.6785]
Ribas, I. 2009, Proc. Int. Astron. Union, 5, 3
Robertson, P., Endl, M., Cochran, W. D., & Dodson-Robinson, S. E. 2013, ApJ, 764, 3
Roccetti, G., Sterzik, M. F., Seidel, J. V., et al. 2025, A&A, 700, A62
Rukdee, S., Buchner, J., Burwitz, V., et al. 2024, A&A, 687, A237
Sairam, L., & Madhusudhan, N. 2025, MNRAS, accepted [arXiv:2503.19908]
Salz, M., Schneider, P. C., Czesla, S., & Schmitt, J. H. M. M. 2015, A&A, 576, A42
Salz, M., Schneider, P. C., Czesla, S., & Schmitt, J. H. M. M. 2016, A&A, 585, L2
Sanz-Forcada, J., Micela, G., Ribas, I., et al. 2011, A&A, 532, A6
Sarkis, P., Henning, T., Kürster, M., et al. 2018, AJ, 155, 257
Schmidt, S. P., MacDonald, R. J., Tsai, S. M., et al. 2025, arXiv e-prints [arXiv:2501.18477]
Schweitzer, A., Passegger, V. M., Cifuentes, C., et al. 2019, A&A, 625, A68
Segura, A., Walkowicz, L. M., Meadows, V., Kasting, J., & Hawley, S. 2010, Astrobiology, 10, 751
Shematovich, V. I., Ionov, D. E., & Lammer, H. 2014, A&A, 571, A94
Shields, A. L., Ballard, S., & Johnson, J. A. 2016, Phys. Rep., 663, 1
Shoda, M., & Takasao, S. 2021, A&A, 656, A111
Shorttle, O., Jordan, S., Nicholls, H., Lichtenberg, T., & Bower, D. J. 2024, ApJ, 962, L8
Simmonds, C., Buchner, J., Salvato, M., Hsu, L. T., & Bauer, F. E. 2018, A&A, 618, A66
Smith, R. K., Brickhouse, N. S., Liedahl, D. A., & Raymond, J. C. 2001, ApJ, 556, L91
Stevenson, K. B., Lustig-Yaeger, J., May, E. M., et al. 2025, arXiv e-prints [arXiv:2508.05961]
Tarter, J. C., Backus, P. R., Mancinelli, R. L., et al. 2007, Astrobiology, 7, 30
Taylor, J. 2025, arXiv e-prints [arXiv:2504.15916]
Tsai, S.-M., Innes, H., Lichtenberg, T., et al. 2021, ApJ, 922, L27
Tsai, S.-M., Innes, H., Wogan, N. F., & Schwieterman, E. W. 2024, ApJ, 966, L24
Tsiaras, A., Waldmann, I. P., Tinetti, G., Tennyson, J., & Yurchenko, S. N. 2019, Nat. Astron., 3, 1086
Tubín-Arenas, D., Krumpe, M., Lamer, G., et al. 2024, A&A, 682, A35
Turbet, M., Ehrenreich, D., Lovis, C., Bolmont, E., & Fauchez, T. 2019, A&A, 628, A12
Van Eylen, V., Agentoft, C., Lundkvist, M. S., et al. 2018, MNRAS, 479, 4786
Van Looveren, G., Güdel, M., Boro Saikia, S., & Kislyakova, K. 2024, A&A, 683, A153
Van Looveren, G., Boro Saikia, S., Herbort, O., et al. 2025, A&A, 694, A310
Vidal-Madjar, A., LecavelierdesEtangs, A., Désert, J. M., et al. 2003, Nature, 422, 143
Watson, A. J., Donahue, T. M., & Walker, J. C. G. 1981, Icarus, 48, 150
Welbanks, L., Nixon, M. C., McGill, P., et al. 2025, arXiv e-prints [arXiv:2504.21788]
Werlen, A., Dorn, C., Burn, R., et al. 2025, arXiv e-prints [arXiv:2507.00765]
Wogan, N. F., Batalha, N. E., Zahnle, K. J., et al. 2024, ApJ, 963, L7
Yan, F., & Henning, T. 2018, Nat. Astron., 2, 714
Youngblood, A., France, K., Loyd, R. O. P., et al. 2016, ApJ, 824, 101
Youngblood, A., France, K., Loyd, R. O. P., et al. 2017, ApJ, 843, 31
Yu, X., Moses, J. I., Fortney, J. J., & Zhang, X. 2021, ApJ, 914, 38
Zhu, E., & Preibisch, T. 2025, A&A, 694, A93
Zieba, S., Kreidberg, L., Ducrot, E., et al. 2023, Nature, 620, 746

Appendix A: `VPLanet` model

We used the `VPLanet` model (Barnes et al. 2020) to evaluate the global impact of X-ray radiation. `VPLanet` performs comprehensive simulations of planetary system evolution over a gigayear timescale. Its modules cover internal, atmospheric, rotational, orbital, stellar, and galactic dynamics. These modules can be coupled to allow for the simultaneous simulation of the evolution of terrestrial planets, gaseous planets, and stars. For the stellar rotation period evolution, we adopted an approach from Matt et al. (2015). It is formulated for the torque exerted on a star due to magnetic braking, which depends on the star's mass, radius, rotation rate, and magnetic field strength. The model provides a framework for predicting stellar rotation periods across stellar masses and ages. It also accounts for the dependence of spin-down rates on stellar mass. Lower-mass stars (e.g., M dwarfs) have longer convective turnover timescales. In this study, we employ various modules to calculate the impact of the reported XUV flux from `VPLanet`, including the `AtmEsc`, `STELLAR`, and `FLARE` modules for simulating atmospheric escape. Atmospheric escape rates depend on a planet's mass, radius, composition, magnetic field, and orbital distance, while stellar spin-down variability also plays a significant role in cumulative mass loss (Watson et al. 1981; Matt et al. 2012; Cohen & Drake 2014; Ketzer & Poppenhaeger 2023). Our initial parameters for the modeling are described in Table A.1. For the planetary structure model, we follow the study of Lehmer & Catling (2017), which shows that hydrodynamic escape during early stellar XUV saturation can explain the transition from gas-enveloped to rocky planets, accounting for the observed radius gap in exoplanet populations. The `AtmEsc` module simulates the escape of planetary atmospheres and the discharge of surface volatiles using energy- and diffusion-limited mechanisms. This module focuses on hydrogen-dominated atmospheres and water vapor-dominated atmospheres. In hydrogen-rich cases, hydrogen escapes first due to diffusive separation, delaying the loss of heavier volatiles. For water vapor atmospheres, the module simulates photolysis, with hydrogen escaping hydrodynamically and dragging oxygen along.

Table A.1. Parameters of star and planets used for the simulation with `VPLanet` for K2-18 and K2-18b.

Parameter	Value
Stellar Mass ($M_\odot$)	0.413
Initial Rotation Period (days)	1.0
Planet's Mass ($M_\oplus$)	8.0
Planet Mass-Radius Model	Lehmer17* / NONE
Planet's Radius (present-day) ($R_\oplus$)	2.38
Planet's Eccentricity	0.2
Planet's Semi-major axis (AU)	0.143
Envelope mass ($M_\oplus$)	0.06
Thermosphere temperature (K)	400
Saturated XUV luminosity fraction	10^{-3}
Initial Age (Myr)	5.0
Flare Energy (erg)	10^{33} to 10^{36}

Notes. Reference *Lehmer & Catling (2017)

The `STELLAR` module in `VPLanet` models key properties of low-mass stars ($M_\star \leq 1.4 M_\odot$), such as rotation rate, bolometric luminosity, XUV luminosity, effective temperature, and stellar radius of gyration. In `VPLanet`, the radius of gyration is used to quantify how a planet's or star's mass is distributed internally, which affects its rotational dynamics. The model relies on Baraffe et al. (2015). The rotation period and X-ray luminosity relation follows a power law with index -2.26 (Magaudda et al. 2020) for non-saturated low mass stars in mass bin $0.4 M_\odot < M_* < 0.6 M_\odot$. The model predicts a X-ray luminosity evolution similar to that shown in Fig. 7, i.e., a factor of several higher than observed at the current epoch. The more sophisticated stellar evolution model with different rotators of CJ+21 and its implied stellar high-energy flux evolution is discussed in Sect. 5.

The `FLARE` model (do Amaral et al. 2022) implemented a power law relationship between flare energy and cumulative flare frequency distribution (number/day; Davenport et al. 2019), which also depends on the stellar type and age. We note that the Davenport et al. (2019) model overestimates superflare rates, as it is based on younger, more active stars, with only about 3% of the catalog consisting of M dwarfs (Davenport 2016). This approach allows for a quantitative assessment of the cumulative XUV energy input from random flare events, which complements the quiescent stellar XUV irradiation under the assumption that the flare frequency distribution in EUV has the same power-law index as the one in the optical. The model assumed flare energies between 10^{33} and 10^{36} erg based on Davenport et al. (2019). The `FLARE` module computes the average XUV for each simulation time-step, integrating from lowest to highest flare energy. We note that the Davenport et al. (2019) model was developed for younger and more active stars than the Sun, with only 3% of the catalog stars (Davenport 2016) being M-stars.

We model K2-18b as a mini-Neptune, adopting the Lehmer & Catling (2017) framework. The framework provides a model to explain the gap in exoplanet sizes, known as the "radius valley," which separates smaller rocky planets from larger mini-Neptunes with gas envelopes. This model simulates how a planet's original hydrogen and helium atmosphere is removed by strong X-ray and extreme ultraviolet (XUV) radiation from its host star. The low XUV radiation environment has important implications for the atmospheres of the exoplanets of K2-18. While multiple mechanisms can drive atmospheric mass loss in exoplanets, the only directly observed contributor to date is high-energy (XUV) irradiation. Observational evidence for other drivers, such as stellar winds or magnetic interactions, remains lacking for this system. Therefore, our analysis focuses on hydrodynamic escape processes, including the energy-limited approximation implemented via `VPLanet` (Barnes et al. 2020) for H_2–H_2O-dominated atmospheres (see Fig. A.1).

In the case of H_2/H_2O-dominated atmospheres, we use the `VPLanet` model. The Mini-Neptune scenario is implemented using the `AtmEsc` module, which simulates atmospheric escape processes, reproducing the results from Lopez & Fortney (2013). It demonstrates how the evolution of a Mini-Neptune's gaseous envelope depends on its core mass, initial envelope mass, and total mass.

We use the `AtmEsc` module of `VPLanet` to provide an overview of atmospheric evolution over time. We note, however, that the energy-limited approach can be quite uncertain and in fact is an order-of-magnitude estimate for the upper limit of the mass-loss rate only, see Krenn et al. (2021) for more details. The result of the model is shown in Fig. A.1. The envelope mass evolves by 5% over 1 Gyr, even when stellar flare contributions are included. This suggests that, despite this evolution with flare contribution, the planet can maintain a significant hydrogen-rich envelope. This resilience supports the potential of habitable

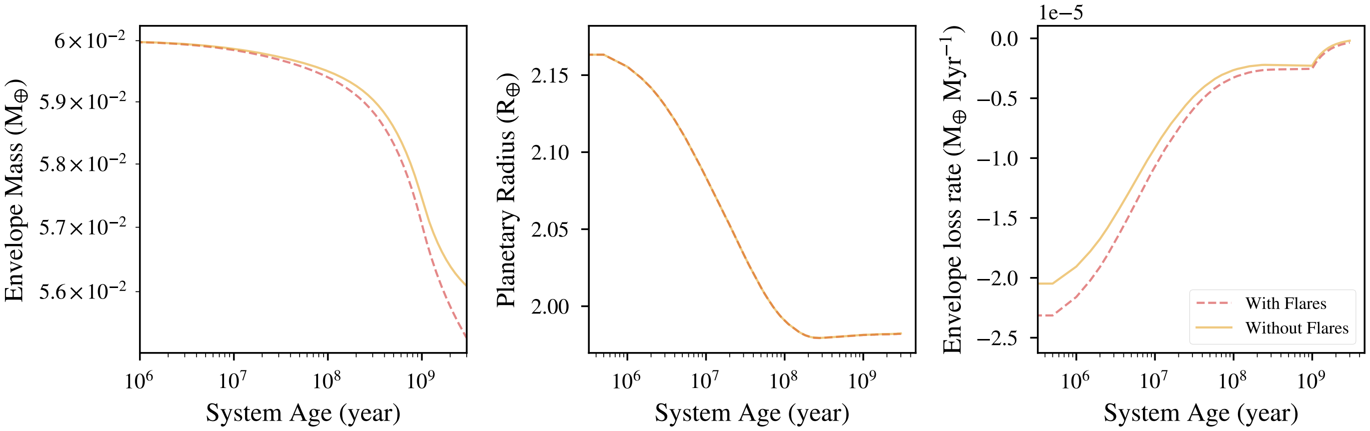

Fig. A.1. Planetary evolution of K2-18b. Left panel: Mass of K2-18b over time. The decrease is following the stellar evolutionary track (see Fig. 7) in the saturated regime, and assuming the system leaves this regime after 1 Gyr. Middle: Evolution of planetary radius. Right: Envelope loss rate. The dashed red line shows the evolution including the flare contribution (do Amaral et al. 2022), while the solid orange line followed the evolution predicted by the `STELLAR` model (Baraffe et al. 2015). Note that the planet radius shown here is limited by the Lehmer & Catling (2017) model.

conditions (liquid water in the form of, for example, surface or subsurface oceans) under a stable envelope in some situations, particularly for so-called Hycean or stratified mini-Neptune models.